

## Magnetoresistance and Fermi Surface Topology of Crystalline Mercury\*

J. M. DISHMAN† AND J. A. RAYNE  
*Carnegie-Mellon University, Pittsburgh, Pennsylvania*

(Received 14 August 1967)

The results of magnetoresistance experiments on a number of oriented single crystals of mercury are reported. Three distinct types of minima are observed in plots of magnetoresistance versus field direction, and these are attributed to open orbits normal to the planes {100}, {011}, and {110}. A unique model of the Fermi surface, formulated in terms of the dimensions of the contact regions on the first zone, is derived to explain these data. An eight-plane-wave pseudopotential calculation including spin-orbit coupling is used to obtain a compensated Fermi surface in substantial agreement with this model and with the first-zone de Haas-van Alphen extremal areas.

### I. INTRODUCTION

UNTIL recently little information concerning the electronic structure of solid mercury has been available, because of the difficulty of preparing oriented single-crystal samples. This problem has been solved over the past few years, and the Fermi surface of mercury has been investigated extensively by means of the de Haas-van Alphen (dHvA) effect.<sup>1</sup> The galvanomagnetic experiments reported here were begun in order to complement the dHvA measurements, and preliminary results have been described elsewhere.<sup>2,3</sup> General agreement is found between these data and those of other workers.<sup>4,5</sup>

There is some difficulty in explaining the galvanomagnetic results on the basis of the model Fermi surfaces thus far proposed for mercury. Both pseudopotential<sup>1</sup> and relativistic-augmented-plane-wave (RAPW) band calculations<sup>6</sup> give agreement with the dHvA areas but fail to predict correctly the angular extent of the experimentally observed open orbits. This has indicated a need for a more thorough investigation of the topological features of possible models for the mercury Fermi surface. Such a study has been carried out, and it has been possible to find a simple four-parameter model which uniquely explains the magnetoresistance data.

In addition to the experimental and topological studies presented, the results of an eight-plane-wave pseudopotential calculation are also given. This calculation includes the effects of compensation and spin-

orbit coupling, and allows a connection to be made between the four-parameter model and the dHvA data. The results of these studies are considered in detail after a brief review of the proposed models for the Fermi surface of mercury.

### II. THEORY

#### A. Fermi-Surface Models

It is helpful by way of introduction to consider several models of the mercury Fermi surface. These models have varying theoretical justification, and it is important to understand what features are essential and what features may be varied in order to produce agreement with both dHvA and magnetoresistance data.

#### 1. Free-Electron Model

Mercury crystallizes normally in the rhombohedral  $\alpha$  phase<sup>7</sup>; the lattice constants and other pertinent data for this phase are found in Table I. The Brillouin zone for this lattice, which is shown in Fig. 1, has been discussed in detail by several authors.<sup>8,9</sup> It is sufficient to recall that it resembles the zone for a fcc lattice, except that it has been stretched along the trigonal axis. This stretching produces three inequivalent types of faces designated *A*, *B*, and *T*, parallel to {100}, {110}, and {111}, respectively, as shown in the figure. The free-electron sphere, appropriate for mercury atoms of valence two, has the same volume as the Brillouin zone and intersects it on the *A* faces as shown by the shaded circles. This intersection produces a two-sheet Fermi surface containing equal volumes of electrons and holes. The first-zone hole surface is open and consists of the unfilled states lying between the surface of the sphere and the zone faces. The second-zone electron surface is comprised of lens-shaped disks lying on the *A* faces of the zone.

\* Work supported by the National Science Foundation. This paper is based on a thesis submitted by one of us (J.M.D.) as partial fulfillment of the requirements for the Ph.D. degree in physics at Carnegie-Mellon University.

† Present address: Bell Telephone Laboratories, Murray Hill, N. J.

<sup>1</sup> G. B. Brandt and J. A. Rayne, *Phys. Rev.* **148**, 644 (1966).

<sup>2</sup> J. M. Dishman and J. A. Rayne, *Phys. Letters* **20**, 348 (1966).

<sup>3</sup> J. M. Dishman and J. A. Rayne, in *Proceedings of the Tenth International Conference on Low-Temperature Physics, Moscow, 1966* (VINITI, Moscow, 1967).

<sup>4</sup> A. E. Dixon and W. R. Datars, *Solid State Commun.* **3**, 377 (1965).

<sup>5</sup> W. R. Datars and A. E. Dixon, *Phys. Rev.* **154**, 576 (1967).

<sup>6</sup> S. C. Keeton and T. L. Loucks, *Phys. Rev.* **152**, 548 (1966).

<sup>7</sup> C. S. Barrett, *Acta Cryst.* **10**, 58 (1957).

<sup>8</sup> M. H. Cohen, *Phys. Rev.* **121**, 387 (1961).

<sup>9</sup> H. Jones, *Theory of Brillouin Zones and Electronic States in Crystals* (Interscience Publishers, Inc., New York, 1960).

## 2. Pseudopotential Models

The pseudopotential model<sup>10</sup> depends on the fact that the effective single-particle wave function (the pseudowave function) is free-electron-like, and can be expressed as a sum of a small number of plane waves. The effective lattice potential (the pseudopotential) enters the calculation through a small number of matrix elements of the form  $\langle \mathbf{k} | W | \mathbf{k} + \mathbf{g} \rangle$  (also known as pseudopotential coefficients or form factors), where  $|\mathbf{k} + \mathbf{g}\rangle$  is a plane-wave state,  $W$  is the pseudopotential, and  $\mathbf{g}$  is a wave-number lattice vector. These matrix elements may be calculated from first principles or they may be used as adjustable parameters to fit the Fermi surface to experimental data, such as the dHvA areas.

To obtain the dHvA model,<sup>1</sup> the latter procedure has been followed using three-plane-wave sets. The change in the first-zone surface is shown schematically in Fig. 2. It can be seen that the main effect of the lattice potential is to introduce contact between the Fermi surface and the  $B$  and  $T$  faces of the Brillouin zone, and to enlarge the already existing regions of contact upon the  $A$  faces. Where the surface contacts the zone, breakthrough regions are created in the hole surface. These openings create the possibility of orbits much smaller than in the free-electron model; e.g., the  $\beta$  orbit is an order of magnitude smaller. Both the  $\beta$  and  $\tau$  orbits shown in Fig. 2 are strongly observed in dHvA experiments. In addition to these closed orbits, the hole surface supports a number of open orbits, two of which are shown in the figure. The existence of these orbits is quite sensitive to the size and shape of the breakthrough regions on the surface. For example, if the plane of an orbit is tilted away from the positions indicated, the trajectory will eventually intersect one of the breakthrough regions. In such a case, the path of motion can fold back upon itself and the previously open orbit becomes closed; this property will be used to deduce an empirical Fermi surface from the magnetoresistance data.

Certain limitations to the dHvA model should be noted. Firstly, divalent mercury is a compensated metal, which implies that the volumes of the hole and electron surfaces should be equal. In the dHvA model the

TABLE I. Crystallographic data for mercury.

Symbol	Value	Remarks
$a_0$	2.9863 Å	Rhombohedral vector at 5°K
$\alpha$	70°44.6'	Rhombohedral angle at 5°K
$g_0$	2.3002 Å <sup>-1</sup>	Magnitude of $\mathbf{g}_{100}$
$\beta$	104°21.7'	Rhombohedral angle for reciprocal lattice
$\Omega$	23.021 Å <sup>3</sup>	Volume of unit cell
$\theta_a$	41.946°	Angle between [100] and [111]
$\theta_v$	65.803°	Angle between $\mathbf{g}_{100}$ and $\mathbf{g}_{111}$
$k_F$	0.59582 $g_0$	Radius of free-electron sphere
$E_F$	0.5240 Ry	Free-electron Fermi energy

<sup>10</sup> W. A. Harrison, *Pseudopotentials in the Theory of Metals* (W. A. Benjamin, Inc., New York, 1966).

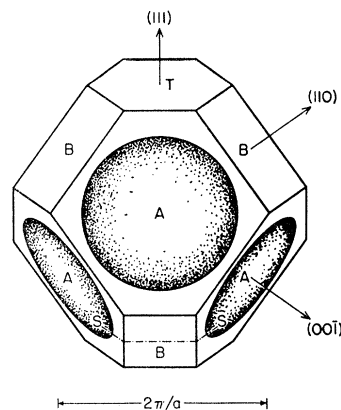


FIG. 1. Brillouin zone of mercury showing intersection of free-electron sphere with the  $A$  faces.

Fermi level was not adjusted to satisfy this requirement, but was simply left at its free-electron value. Secondly, spin-orbit effects were not considered. Since mercury is a heavy element (atomic number 80), it might be expected that spin-orbit coupling is important and should be included explicitly in a pseudopotential calculation.

In most first-principles calculations of the pseudopotential, information about the effect of the core states is obtained from a Hartree-Fock (HF) calculation for the free ion. Heine, Abarenkov, and Animalu (HAA)<sup>11-14</sup> have shown that this information can also be obtained from spectroscopic data on the atomic energy levels for a number of elements, including mercury. Animalu<sup>15</sup> has shown how to include the effect of spin-orbit coupling for these elements. Since all the required theoretical parameters are available in the form of tables,<sup>10</sup> it is a straightforward matter to calculate the energy bands for mercury using this procedure. Such a

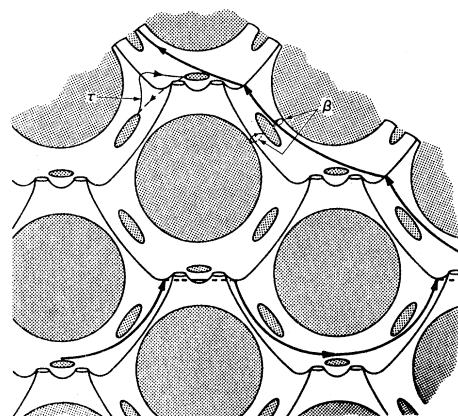


FIG. 2. Schematic representation of the first-zone Fermi surface of mercury showing the location of typical open and closed orbits.

<sup>11</sup> I. Abarenkov and V. Heine, *Phil. Mag.* **12**, 529 (1965).

<sup>12</sup> V. Heine and I. Abarenkov, *Phil. Mag.* **9**, 451 (1964).

<sup>13</sup> A. O. E. Animalu and V. Heine, *Phil. Mag.* **12**, 1249 (1965).

<sup>14</sup> A. O. E. Animalu, *Phil. Mag.* **11**, 379 (1965).

<sup>15</sup> A. O. E. Animalu, *Phil. Mag.* **13**, 53 (1966).

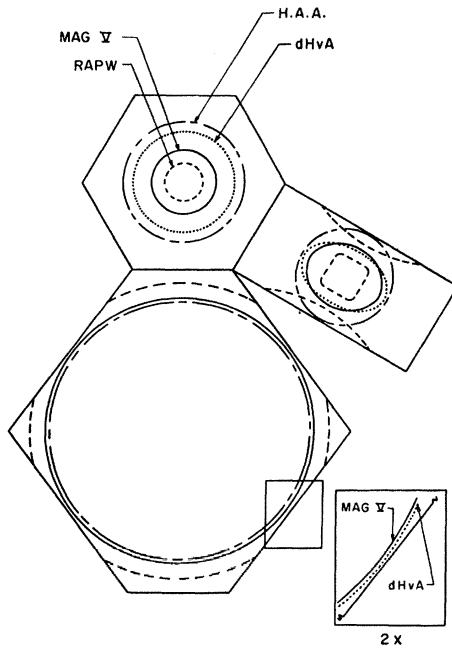


FIG. 3. Relative sizes of the contact regions for four models of the first-zone Fermi surface. Simple shapes are used to approximate the actual contact regions. The inset shows the relation of the dHvA and MAG V contact regions on the  $A$  face.

calculation has been carried out using eight plane waves of the form  $|\mathbf{k} + \mathbf{g}, \alpha\rangle$ ,  $|\mathbf{k} + \mathbf{g}, \beta\rangle$ , where  $\mathbf{g} = 0$ ,  $\mathbf{g}_{001}$ ,  $\mathbf{g}_{011}$ ,  $\mathbf{g}_{111}$ , and  $\alpha, \beta$  are spin indices. In addition, the Fermi level has been adjusted to give a surface which is approximately compensated, using the technique of Harrison.<sup>10</sup> The resulting Fermi surface is topologically equivalent to that of the dHvA model, but the breakthrough regions on the  $B$  and  $T$  faces are much larger. A comparison of the dimensions for the various models considered is given in Table II and Fig. 3.

### 3. Relativistic-Augmented-Plane-Wave Model

The RAPW method,<sup>16,17</sup> which automatically includes the expected large relativistic effects, produces a Fermi surface topologically equivalent to the two previously discussed.<sup>2</sup> As compared to the dHvA model, there is

TABLE II. Breakthrough dimensions of first-zone hole surface.<sup>a</sup>

Model	Breakthrough dimension (units of $g_0$ )			
	$r_A$	$r_T$	$a_B$	$b_B$
dHvA	0.390	0.141	0.079	0.130
RAPW	0.412	0.051	0.050	0.051
HAA	0.361	0.166	0.151	0.152
MAG V	0.374	0.086	0.091	0.113
8 PW	0.380	0.031	0.091	0.077

<sup>a</sup> Dimensions  $r_A$  and  $r_T$  are radii of circular approximations to the breakthrough regions on the  $A$  and  $T$  faces, respectively. Dimensions  $a_B$  and  $b_B$  are semiminor and semimajor axes, respectively, of the elliptical approximation to the breakthrough region on the  $B$  face.

<sup>16</sup> T. L. Loucks, Phys. Rev. **139**, 1333 (1965).

<sup>17</sup> T. L. Loucks, Phys. Rev. **143**, 506 (1966).

improved agreement between the observed and calculated extremal dHvA areas, although the  $\tau$  orbit is still about 15% smaller than the observed value. The most striking topological feature of the model as compared to the others is the very large breakthrough region on the  $A$  faces of the zone. This breakthrough is so large, in fact, that it overlaps the edge of the face to form an indented region on the  $B$  faces (see Fig. 3). The other contact regions, however, are smaller in comparison with previous models. It should be noted that the Fermi energy chosen to produce this surface has been determined by requiring the calculated and observed areas for the  $\beta$  orbit to be in exact agreement. There may thus be a lack of compensation in this model, since it is not certain that the electron and hole volumes are equal.

By way of summary, it can be said that the three theoretical models considered are topologically similar in that they all give rise to closed orbits observed in the dHvA experiments, and to open orbits seen in magnetoresistance measurements. All show contact between the Fermi surface and each of the zone faces. The differences in the three models concern the precise size and shape of these contact regions; it is the determination of the extent of these regions where the magnetoresistance is expected to be useful.

### B. Magnetoresistance Theory

As originally shown by Lifshitz, Azbel, and Kaganov,<sup>18</sup> the galvanomagnetic properties of a metal in the high-field limit can be understood independently of the detailed electronic scattering mechanisms and solely in terms of the geometry of the Fermi surface. Pippard<sup>19</sup> and Fawcett<sup>20</sup> have reviewed this subject in detail, and only the results applicable to mercury will be recalled here.

Simply stated, the magnetoresistance for a metal in the high-field limit is expected either to rise quadratically with field, or to saturate independently of field, depending upon which of a set of conditions is satisfied. These conditions for a compensated metal such as mercury are given in Table III. Conditions I and II imply that open orbits are distinguished from closed orbits only if the current direction is favorably oriented with respect to the crystal axes of the sample. Thus the angle  $\alpha$  between the open-orbit direction in  $\mathbf{k}$  space and the current direction should be close to  $90^\circ$ , so that the term quadratic in the field is small and the magnetoresistance saturates. This condition imposes important restrictions upon sample preparation for these experiments.

<sup>18</sup> I. M. Lifshitz, M. I. Azbel, and M. I. Kaganov, Zh. Eksperim. i Teor. Fiz. **31**, 63 (1965) [English transl.: Soviet Phys.—JETP **4**, 41 (1957)].

<sup>19</sup> A. B. Pippard, *Les Houches Lectures on Low Temperature Physics* (Gordon and Breach Science Publishers, Inc., New York, 1965).

<sup>20</sup> E. Fawcett, Advan. Phys. **13**, 139 (1964).

Saturation is also obtained if condition III is satisfied, which will be the case, for a particular orientation of the field, if different planes normal to the field intersect the Fermi surface so as to produce open trajectories having different directions. Such field directions might be present at points on the stereogram where two one-dimensional regions of open orbits cross. Condition IV, which also leads to saturation, is satisfied for field directions where closed orbits of one character (e.g., electrons) are excited on an open sheet of the opposite character (e.g., a hole surface). In addition, these closed orbits must not be enclosed by larger orbits with the same character as the open sheet, nor may any open orbits be excited. Such singular-field directions are usually associated with an axis of higher than two-fold symmetry, located at the center of a two-dimensional region of the stereogram where a periodic open orbits are excited. For compensated metals the equality of holes and electrons is destroyed for these directions, giving rise to geometric discompensation.<sup>20</sup>

### III. EXPERIMENT

#### A. Sample Preparation and Experimental Equipment

A number of oriented single-crystal specimens have been prepared for use in the magnetoresistance experiments. To prevent damage during handling, these samples are grown in epoxy molds suitably prepared to allow the attachment of current and voltage leads. The latter consist of 36-gauge copper wire, amalgamated with mercury on one end, and soldered to the sample on the surface of the supporting molds, where the mercury is exposed during growth. Each sample has been oriented to within  $\frac{1}{2}^\circ$  by back-reflection Laue techniques.

A standard four-terminal method has been used for measuring the magnetoresistance. With a constant current of 600 mA applied to the two outer terminals of the sample, the voltage across the two inner terminals is monitored by an Astrodata Model 121Z nanovoltmeter, the output of which is connected to the *Y* axis of a Moseley 2D2 *X-Y* recorder. Rotation diagrams are obtained at a fixed field magnitude as the magnet is rotated about the sample, and the *X* axis is driven by a voltage indicating the field direction. In these experiments, the sample is mounted in a supporting probe, which utilizes a worm gear to tilt the sample in a plane normal to the plane of rotation of the magnet. This tilting mechanism, which is similar to those described by other workers,<sup>21</sup> is capable of rotating the sample through an angle of  $270^\circ$ . By a combination of tilting and magnet rotation, all inequivalent directions of the mercury stereogram can be investigated for any sample. Calibration of the tilting mechanism allows the sample orientation to be set to an accuracy of  $0.1^\circ$ . All the tilting experiments have been performed for fields up to 11 kG, and at a temperature of  $1.2^\circ\text{K}$ . This field is

<sup>21</sup> D. J. Sellmyer, Rev. Sci. Instr. 38, 434 (1967).

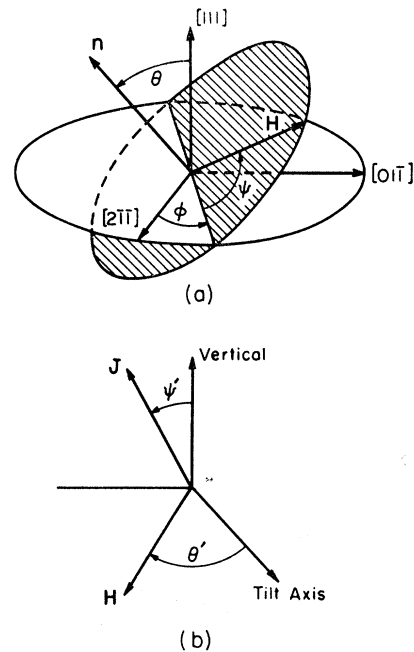


FIG. 4. (a) Definition of the Eulerian transformation locating the position of *H* with respect to the crystal axes; (b) definition of the tilt and rotation angles,  $\psi'$  and  $\theta'$ , respectively, for the geometry used in the tilting experiments.

found to be more than sufficient to achieve the high-field limit, the minima being only slightly reduced from those observed at 30 kG with the current axis fixed.

#### B. Results

Results for three representative samples are presented here; several general features are common to all. As expected for a compensated metal, the magnetoresistance is large for most field directions with a field dependence of  $H^m$ , where  $m=1.92$ . This slight deviation from quadratic behavior has been observed for other compensated metals.<sup>20</sup> A second feature is the occurrence of minima in the rotation diagrams for the various samples. When the field positions giving rise to these features are plotted on a stereogram, it is found that they all lie on one or another of great circles (one-dimensional regions) representing planes of the mercury lattice. Two kinds of dips in the magnetoresistance are observed: (1) deep, narrow minima with field positions in low-index planes, either  $\{100\}$ ,  $\{1\bar{1}0\}$ , or  $\{110\}$ ; (2)

TABLE III. Field dependence of magnetoresistance for a compensated metal.

Condition	Magnetoresistance
I. Closed orbits	$\Delta\rho/\rho \sim H^2$
II. Open orbits in one direction	$\Delta\rho/\rho \sim H^2 \cos^2\alpha + H^0 \sin^2\alpha$
III. Two nonintersecting bands of open orbits	$\Delta\rho/\rho \sim H^0$
IV. Singular field direction	$\Delta\rho/\rho \sim H^0$

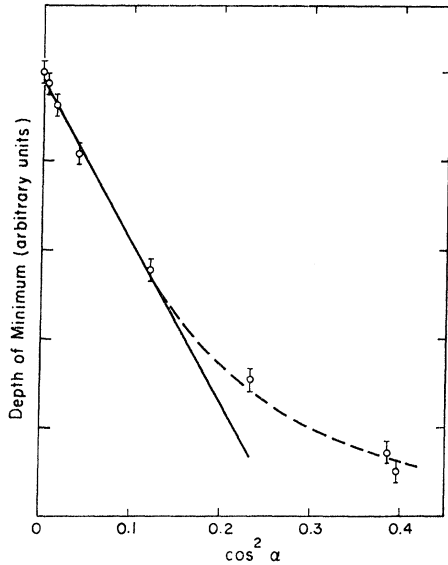


FIG. 5. Plot of the depth of the minimum corresponding to  $H$  along  $[01\bar{1}]$  versus the angle between  $g_{100}$  and the current direction, for a number of transverse magnetoresistance samples.

less pronounced minima with field positions in higher index planes, or planes incommensurable with the crystal lattice.

To discuss the results and their interpretation, it is convenient to set up a coordinate system within the mercury lattice and to designate the field positions where minima occur by means of an Eulerian transformation with respect to this system. Figure 4(a) shows the axes used: the bisectrix  $[2\bar{1}\bar{1}]$ , the binary  $[01\bar{1}]$ , and the trigonal  $[111]$ . The normal to the plane in which the minimum occurs is obtained by rotations through angles  $\phi$  and  $\theta$ , respectively, and the field position in this plane relative to the basal plane is

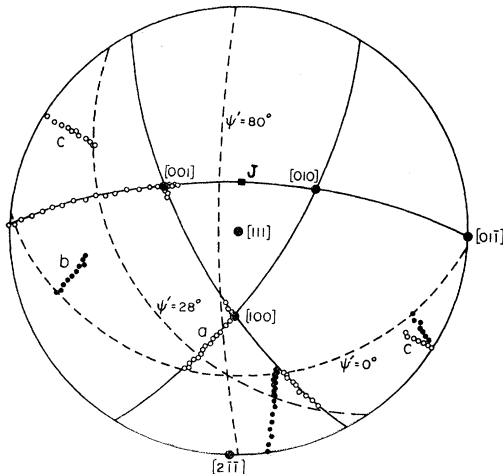


FIG. 6. Stereographic plot of the field positions giving rise to minima in the rotation diagrams for a sample with  $J$  specified by  $\phi = 89^\circ$ ,  $\theta = -24^\circ$ , and  $\psi = -86^\circ$ . Open circles indicate positions of narrow minima, solid circles indicate positions of broad minima.

measured by  $\psi$ . The Eulerian convention used here is that used by Goldstein,<sup>22</sup> and for convenience all angles are defined in the range  $-90^\circ$  to  $+90^\circ$ . For example, the minimum occurring when the field lies along  $[010]$ , which is in the  $(100)$  plane, is designated by  $\phi = 90^\circ$ ,  $\theta = 65.80^\circ$ ,  $\psi = 54.63^\circ$ .

To describe the rotation diagrams, the notation defined in Fig. 4(b) will be used. The nature of the experimental geometry is such that one axis of the crystal remains fixed in the plane of the magnet rotation, while the current direction is tipped from the vertical to the horizontal. The tilt angle about this axis is denoted by  $\psi'$  and the field position relative to the tilt axis is denoted by  $\theta'$ . In order to indicate the position of the tilt axis for a given sample with respect

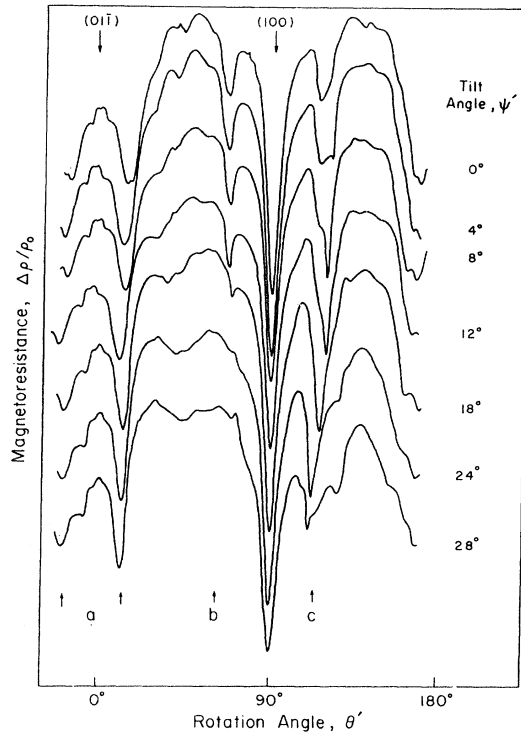


FIG. 7. Rotation diagrams for the sample with  $J$  given by  $\phi = 89^\circ$ ,  $\theta = -24^\circ$ , and  $\psi = -86^\circ$ , and with tilt angles  $\psi'$  from  $0$  to  $28^\circ$ . The zero of each diagram has been shifted for convenience of reproduction.

to crystal axes, the Eulerian transformation above can be used, the tilt-axis direction being substituted for the magnetic-field direction.

Transverse magnetoresistance measurements have been made on a number of samples, all with current axes lying in the mirror plane  $(01\bar{1})$ . The experimental geometry for these studies has been arranged so that the rotation diagram for each sample includes a field position lying along  $[01\bar{1}]$ . A deep minimum centered

<sup>22</sup> Herbert Goldstein, *Classical Mechanics* (Addison-Wesley Publishing Co., Inc., Reading, Mass., 1959), pp. 109ff.

about this field direction is observed for each sample, the depth of the minimum varying with the angle  $\alpha$  between the current axis and the normal to (100) as shown in Fig. 5. For  $\alpha$  near  $90^\circ$  the depth of the minimum is seen to change linearly with  $\cos^2\alpha$ , as expected if it is due to an open orbit normal to (100). It should be noted here that the free-electron model predicts the existence of another set of open orbits, normal to (011), for this field direction. In this case the magnetoresistance should saturate independently of the value of  $\alpha$  (Table III, condition III). The observed dependence, shown in Fig. 5, is contradictory to this result and indicates such orbits do not exist.

The results of several of the tilting experiments are shown in Figs. 6-8. Each stereogram indicates the

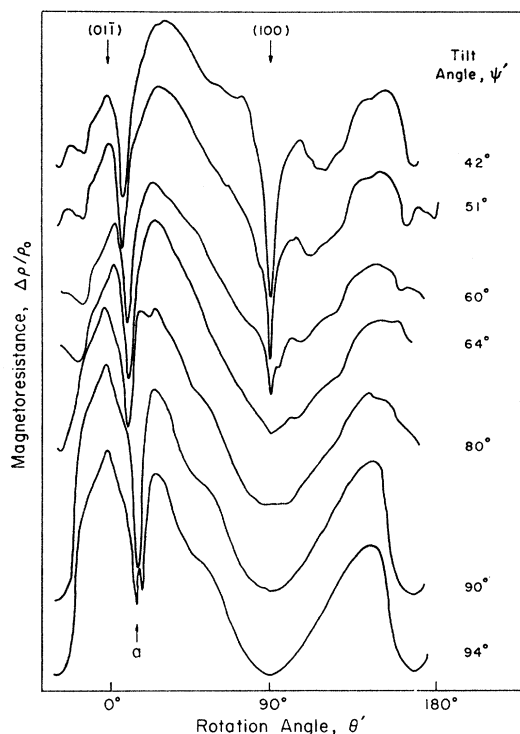


FIG. 8. Rotation diagrams for the sample with  $\mathbf{J}$  given by  $\phi = 89^\circ$ ,  $\theta = -24^\circ$ , and  $\psi = -86^\circ$ , and with tilt angles  $\psi'$  between  $42^\circ$  and  $94^\circ$ .

field positions where minima have been observed, the locations of representative rotation diagrams, and the position of the current direction for a given crystal. The other figures give examples of the rotation diagrams obtained, with the zero-resistance position of each diagram shifted for convenience of reproduction. The crystal corresponding to Fig. 6 is seen to have a current direction particularly suitable for observing open orbits whose directions lie along the reciprocal lattice vectors  $\mathbf{g}_{100}$  and  $\mathbf{g}_{011}$ . For this sample the tilt axis lies along the direction given by  $\phi = 89^\circ$ ,  $\theta = -24^\circ$ , and  $\psi = -86^\circ$ , and it is common to all the rotation diagrams in Figs. 7 and

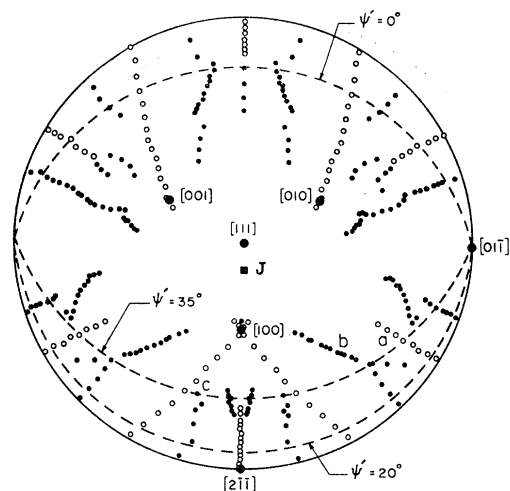


FIG. 9. Stereographic plot of the field positions giving rise to minima in the rotation diagrams for the sample with  $\mathbf{J}$  specified by  $\phi = 0^\circ$ ,  $\theta = 90^\circ$ , and  $\psi = 76^\circ$ .

8 for  $\theta' = 0^\circ$ . The most prominent dip in the magnetoresistance occurs for  $\mathbf{H}$  lying in (100) at  $\theta' = 90^\circ$ . This feature is seen to vanish for  $\psi' = 63^\circ$ , where it is replaced by a very broad trough resulting from the approach to longitudinal magnetoresistance at  $\psi' = 90^\circ$ . Minima arising for field positions in (010) and (001) are indicated by the  $a$  positions in Figs. 6, 7, and 8. These two planes intersect at  $[100]$  and the deep drop in magneto-

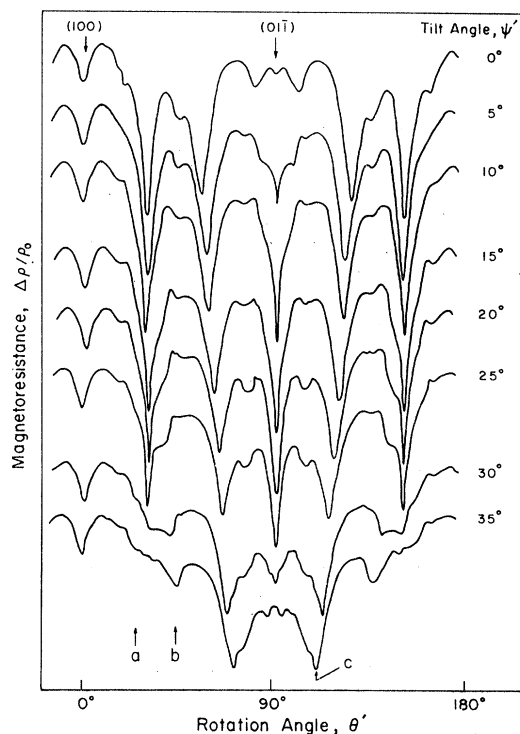


FIG. 10. Rotation diagrams for the sample with  $\mathbf{J}$  specified by  $\phi = 0^\circ$ ,  $\theta = 90^\circ$ , and  $\psi = 76^\circ$ .

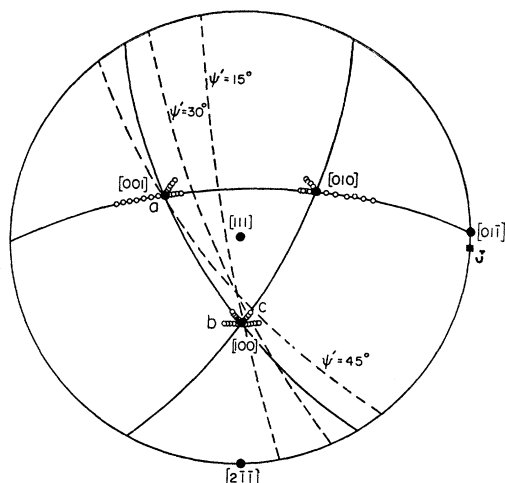


FIG. 11. Stereographic plot of the field positions giving rise to minima in the rotation diagrams for the sample with  $\mathbf{J}$  given by  $\phi=0^\circ$ ,  $\theta=0^\circ$ , and  $\psi=87^\circ$ .

resistance for the field in this position is seen in Fig. 8 for  $\psi'=90^\circ$ . That this feature is related to both the planes is illustrated by the rotation diagram for  $\psi'=94^\circ$ , where the minimum has split into two parts corresponding to the field crossing (010) and (001) separately. Since  $\alpha=55^\circ$  for these orbits, their associated minima are not as deep as for (100).

A prominent, but shallow, set of minima is observed at the position  $b$  in Figs. 6 and 7. These dips arise from the field lying in (210) and vanish for  $\psi'=20^\circ$ . A similar set occurs at the position  $c$ , but in this case additional structure is seen for  $\psi'\geq 4^\circ$ . The reason for this behavior is seen by inspection of Fig. 6, where it is shown that for these tilt angles the plane of the field rotation intersects (201) and (110) at positions having only slightly different rotation angles  $\theta'$ . The appearance of the sharp structure on the right side of these features in Fig. 7 is attributed to the excitation of open orbits along  $[1\bar{1}0]$ , for which  $\alpha=69^\circ$ , while the broader portion of these minima is associated with the field lying in (201). It should be noted that the selection of tilt axis for this sample does not allow the field to be oriented arbitrarily in either (210) or (201). However, those directions not investigated in (210) are covered by sweeps through the equivalent plane, (201), so that the minima at  $b$  form a continuation of those observed at  $c$ . The features at  $b$  and  $c$  illustrate the distinction made between the open and solid circles in the stereograms of Figs. 6, 9, and 11. The dips associated with the open circles are quite sharp and sometimes deep, while those associated with the solid circles are much broader and shallower.

It will be noted from Fig. 6 that the plane of field rotation intersects  $(01\bar{1})$  only over a limited range due to the selection of tilt axis for this sample. Thus, although the current direction is favorable for observing orbits normal to this plane, a set of minima for these

orbits are not seen in the diagrams shown. Their effect is seen only for  $\psi'=90^\circ$ , in which case the field is rotated very nearly in  $(01\bar{1})$  giving rise to the very broad and deep depression near  $\theta'=180^\circ$ . Its breadth gives an indication of the extent over which open orbits exist in  $(01\bar{1})$ . They are more precisely observed in the crystal studied in Figs. 9 and 10.

The mirror symmetry of the diagrams shown in Fig. 10 about the positions  $\theta'=0^\circ$  and  $\theta'=90^\circ$  results from the fact that the current axis for this sample lies precisely in the mirror plane, and the experimental geometry is such that each rotation diagram corresponds to the field being rotated in a plane normal to  $(01\bar{1})$ . For this sample the tilt axis lies along  $[01\bar{1}]$ , and is common to each rotation diagram, producing the minimum for  $\theta'=0^\circ$ . This feature is attributed to open orbits normal to (100) for which  $\alpha=52^\circ$ , thus explaining its small depth.

A prominent set of minima in this sample is seen to arise for the field in  $(01\bar{1})$  with  $\theta'=90^\circ$ . These depressions vanish for  $\psi'=4^\circ$  and  $\psi'=30^\circ$ , the cutoff in the latter position being quite sharp with the minimum replaced by a local maximum. The cutoff in the other position is more gradual and a vestige of the minimum remains, as shown in the diagram for  $\psi'=0^\circ$ . Approximately  $15^\circ$  on either side of this feature are observed small, subsidiary dips, which become more prominent as the  $(01\bar{1})$  minima vanish. They are quite well resolved for  $\psi'=0^\circ$  and they seem to form the shoulder

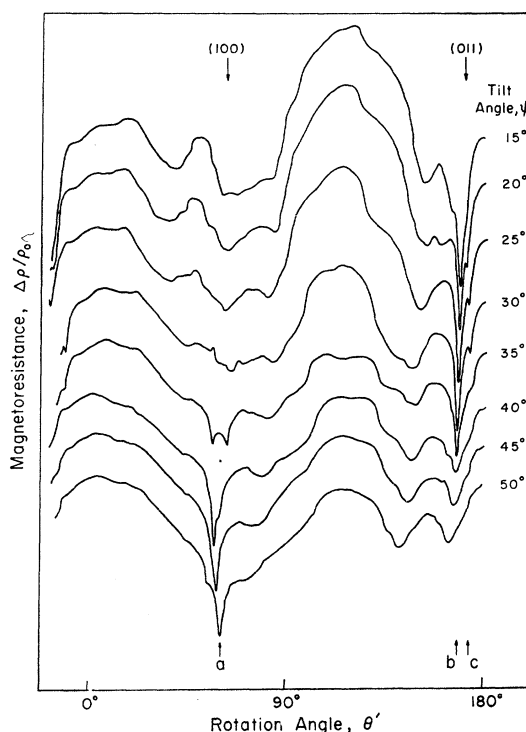


FIG. 12. Rotation diagrams for the sample having  $\mathbf{J}$  given by  $\phi=0^\circ$ ,  $\theta=0^\circ$ , and  $\psi=87^\circ$ .

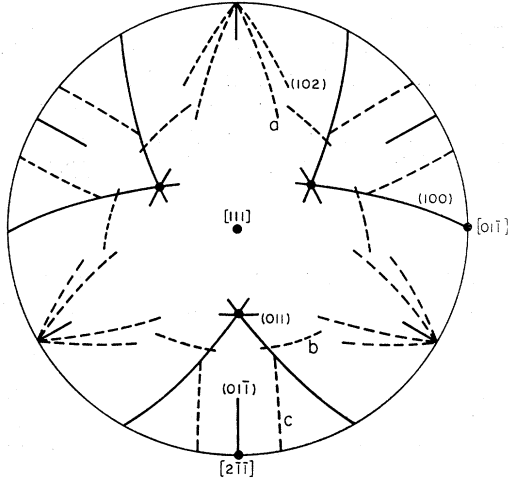


FIG. 13. Summary of field positions giving rise to minima for all samples measured. Solid lines indicate the positions of narrow minima, dashed lines indicate the positions of broad minima.

of the minima labeled *c* in Fig. 10. These depressions and their mirror images arise for the field in (010) and (001); for open orbits normal to these planes,  $\alpha = 57^\circ$ . Troughs arising for the field in the other mirror planes of the sample are shown at position *a* and its mirror image. As for the previous sample, these minima seem to be composed of a deep part and a broad shoulder. The latter is resolved into a separate minimum when the mirror-plane minima have been cut off, as indicated by position *b* for tilt angles  $\psi' = 25^\circ, 30^\circ, \text{ and } 35^\circ$ , and it appears for field positions lying very close to  $(\bar{1}25)$ .

Figures 11 and 12 indicate the data obtained for a sample with current axis very close to  $[01\bar{1}]$ . As compared to the other samples, the rotation diagrams show less structure owing to the fact that  $\alpha$  is favorable only for observing orbits with the field in (100) and (011). The set of minima arising from field positions in (011) are indicated by position *b* in Fig. 12. These minima are quite narrow and deep, but there is difficulty in deciding for which tilt angle they vanish. The depression for  $\psi' = 35^\circ$  is quite pronounced, while for  $\psi' = 40^\circ$  it has broadened considerably; yet even for  $\psi' = 50^\circ$  some sort of minimum still appears for **H** in (011).

The features at position *c* arise for field positions in (001). They are observed only over a small range, since the current axis is not favorable ( $\alpha = 37^\circ$ ) for their appearance. Their cutoff at  $\psi' = 35^\circ$  is in agreement with the cutoff positions observed for these minima in other crystals. The orbits responsible for these minima are also seen for **H** lying in (100) at position *a*. The splitting of this minimum for  $\psi' = 35^\circ$  and the appearance of a shoulder for  $\psi' = 40^\circ$  arises from the field being swept through (110), which lies very close to (100) for these tilt angles. These two planes intersect at  $[001]$ , and the field in this direction produces the deep depression observed for  $\psi' = 45^\circ$ .

The field dependence for directions giving rise to the various minima in the magnetoresistance has been studied, but the results are rather inconclusive. For the deep depressions, the magnetoresistance is very low, and the field dependence can be observed only by increasing the gain of the nanovoltmeter. When this is done, the signal-to-noise ratio becomes very low, obscuring the shape of the recorder traces. For some of the better oriented crystals examined in the transverse magnetoresistance experiments, it appears that deviation from quadratic behavior begins to occur for the maximum available fields, i.e., 29 kG. For the singular field direction,  $[100]$ , where the current orientation is not critical for observing saturation, this deviation from quadratic behavior seems to occur at 11 kG and a definite inflection point is noted. In this case, however, there is some difficulty in aligning the field precisely along  $[100]$ , so that saturation is never observed. For the shallower minima investigated, the field dependence is very nearly quadratic.

A summary of the field positions where minima have been observed for all the crystals investigated is shown in Fig. 13. The solid lines in the figure indicate the positions of the deep minima, while the dashed lines indicate the location of the less pronounced depressions. Table IV summarizes the location, angular range, and cutoff sharpness for the different types. The latter parameter refers to range over which the minimum vanishes and its determination involves some arbitrariness, since the depth of the minima for the field in a given plane decreases quite rapidly over a range of several degrees near the cutoff position. If it is assumed that no information can be obtained about the existence of open orbits for this angular range, then the cutoff

TABLE IV. Angular range of magnetoresistance minima.

Minima type	Range	Cutoff sharpness
{100}	$\phi = 90^\circ$ $\theta = 65.8^\circ$ $-63.2^\circ \leq \psi \leq 63.2^\circ$	$\pm 0.2^\circ$
{01 $\bar{1}$ }	$\phi = 0^\circ$ $\theta = 90^\circ$ $-9.9^\circ \leq \psi \leq 16.0^\circ$	$\pm 0.4^\circ (\psi = -9.9^\circ)$ $\pm 0.2^\circ (\psi = 16.0^\circ)$
{011}	$\phi = 90^\circ$ $\theta = -48.1^\circ$ $-99.6^\circ \leq \psi \leq -80.4^\circ$	$\pm 0.4^\circ$
{102}	$\phi = 0^\circ$ $\theta = 52.1^\circ$ $-32.2^\circ \leq \psi \leq 0^\circ$	...
<i>a</i>	$\phi = 0^\circ$ $\theta = 63^\circ$ $-39^\circ \leq \psi \leq 0^\circ$	...
<i>b</i>	$\phi = 84^\circ$ $\theta = -33^\circ$ $62^\circ \leq \psi \leq 85^\circ$	...
<i>c</i>	$\phi = 10^\circ$ $\theta = 80^\circ$ $0^\circ \leq \psi \leq 29^\circ$	...



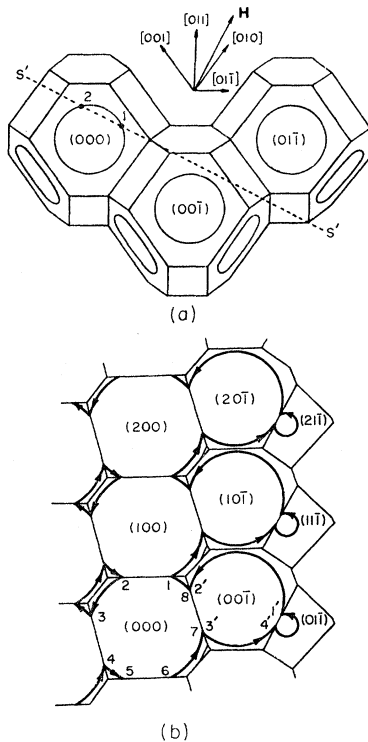


FIG. 14. (a) View of the repeated zone scheme with the (100) zone faces parallel to the plane of the figure. Line  $S'S'$  shows the position of an orbit plane normal to both the plane of the figure and to  $\mathbf{H}$ . (b) Section  $S'S'$  of the repeated zone scheme showing fifth-order open orbit for free-electron model.

sharpness is just equal to the range itself. It is on the order of  $4^\circ$  for the four cutoff positions in  $\{100\}$ ,  $\{01\bar{1}\}$ , and  $\{011\}$ . On the other hand, if it is assumed that open orbits still exist throughout the range of rapid decrease of the minima depth, then the cutoff sharpness is on the order of  $1^\circ$ . The latter assumption has been made in obtaining the numbers in Table IV.

The data reported here are in general agreement with that obtained by Datars and Dixon. Well-resolved minima, not previously reported, are observed in  $\{102\}$  and in the regions  $a$  and  $c$  of Fig. 13. The region  $b$  would appear to correspond to the minima which they have observed in  $\{213\}$ . This set was not well resolved in the experiments reported here, and the features were so broad that they could not be assigned definitely to  $\{213\}$  planes. The set of minima corresponding to  $c$  seem to lie in planes incommensurable with the crystal lattice. They are well resolved, particularly in the sample of Fig. 6 and would appear to be connected with the discontinuity observed in the dHvA data for these field directions.<sup>1</sup> A number of small depressions, not shown in Fig. 13, are plotted as solid circles in Fig. 9. Their positions compare favorably with the subsidiary minima shown by Datars and Dixon. For both experiments the angular ranges observed for the three principal types of minima in  $\{100\}$ ,  $\{1\bar{1}0\}$ , and  $\{110\}$  agree to within the combined error. The un-

certainty in these ranges is larger for their measurements than those given here, but this may be due at least in part to the interpretation of the cutoff point. The major differences between their work and that reported here lie in the interpretation of some of the observed minima, as will shortly become apparent.

#### IV. OPEN-ORBIT CALCULATION

To interpret the magnetoresistance data further, a search must be carried out to locate all possible open orbits, their type and angular extent for each model of the mercury Fermi surface. This investigation can best be carried out by means of a digital computer. The qualitative method of the computer search program and the results for several models are discussed below.

##### A. Open-Orbit Search Method

Even in the absence of a simple model for the first zone sheet of the mercury Fermi surface, it is apparent that whatever its detailed shape, it will be based upon a framework of Brillouin zones constructed in the repeated or periodic zone schemes,<sup>10</sup> i.e., where the zones are stacked together in a regular array, filling all of  $\mathbf{k}$  space. Each zone in this scheme contains an identical portion of the Fermi surface, the latter being connected from zone to zone by the contact regions on the zone faces. It is the relation of these contact regions on the various zone faces in the repeated zone scheme that is the primary factor determining the existence of open orbits. To a first approximation, it does not matter how the carrier moves within a zone, but only if it can travel from one zone to another without returning to its starting point. If it can do this while remaining in a single orbit plane, then an open orbit exists for a field direction normal to this plane.

The manner in which the open-orbit search program functions can be explained most easily with the help of Fig. 14. For a given field direction, 200 possible orbit planes equally spaced across the width of one Brillouin zone are considered. One such plane, normal to the plane of the page, is shown in Figure 14(a) by the line  $S'S'$ . The coordinates of  $\mathbf{H}$  normal to this plane are  $\phi=90^\circ$ ,  $\theta=65.80^\circ$ ,  $\psi=63^\circ$ , the intersection of this plane with the zones of the repeated zone scheme being shown in Fig. 14(b). The origin of  $\mathbf{k}$  space is taken to lie at the center of one of the zones, labeled (000) in the figure. For each of the 14 faces of the zone a simple shape is assumed for the contact region on that face. The search program then finds the simultaneous solution (possibly imaginary) between the equation representing the shape of the contact region and the equation of the orbit plane. Real solutions represent the intersections of the orbit plane and the contact region; for example, in the (000) zone of Fig. 14 there are eight such intersection points. One of these points, say 7, is taken to be the starting point of the orbit tracing. Since this point lies

on the  $(00\bar{1})$  face of zone  $(000)$ , the carrier will exit across this face and enter zone  $(00\bar{1})$ . Now the solutions for the orbit plane and the 14 faces of this zone are found, in this case there being four intersection points. The program finds that point  $3'$  corresponds to point 7, and is thus the entrance point. To find the exit point it investigates the angular relation of point  $3'$  to the other intersection points. Since there are more than two intersection points, it knows that  $2'$  cannot be the exit point, since it lies on the same face as  $3'$ ; therefore, the exit point is  $4'$ . This point lies on the  $(010)$  face of zone  $(00\bar{1})$ , and hence the carrier exits across this face into zone  $(01\bar{1})$ . Here, there are only two intersection points, so the carrier returns to the  $(00\bar{1})$  zone across the  $(010)$  face. As each exit point is found, the program asks if it is the starting point (point 7). If the answer is in the affirmative, then a closed orbit has been found; otherwise the process continues until twelve zones have been traversed. In the example shown, the orbit would be traced until it reached the  $(21\bar{1})$  zone. If point 2 had been the starting point, the indicated closed orbit would have been found after four traverses. Although Fig. 14(b) indicates schematically the path of the orbit by means of the arcs shown, it should be pointed out that the search program considers only the coordinates of points on the zone faces. No intermediate points inside the zone are used. As the orbit is traced in this fashion, various information concerning its approximate arc length and direction is printed out.

Two major assumptions made by the search program should be mentioned. First, for simplicity, it is assumed that the contact regions on the zone faces are elliptically shaped. This allows the contact to be described in a simple way mathematically, and introduces a small number of parameters to describe the dimensions of these regions, namely, the semimajor and semiminor axes of the ellipses. Symmetry considerations require that the contact areas on the  $A$  and  $T$  faces be circles. Thus the total number of parameters needed to describe the contact is four, viz., the radii of the circles on the  $A$  and  $T$  faces, designated  $r_A$  and  $r_T$ , respectively, and the two axes of the ellipse on the  $B$  face. The intercept of this ellipse along the symmetry line  $XK$  will be denoted by  $a_B$ , and the intercept along the symmetry line  $XU$  will be denoted by  $b_B$  (see Fig. 20 for the symmetry points of the mercury Brillouin zone). This assumption of elliptically shaped contact regions is supported by the shape of these areas for the RAPW and pseudopotential models.

The second assumption made concerns the connectivity of the Fermi surface from zone to zone. Since the program does not consider the topology of the surface within each zone, but only uses the size and shape of the contact regions on the zone faces, it is being tacitly assumed that the surface is connected from one zone to the next like two intersecting spheres. In actuality the surface is distorted by the lattice

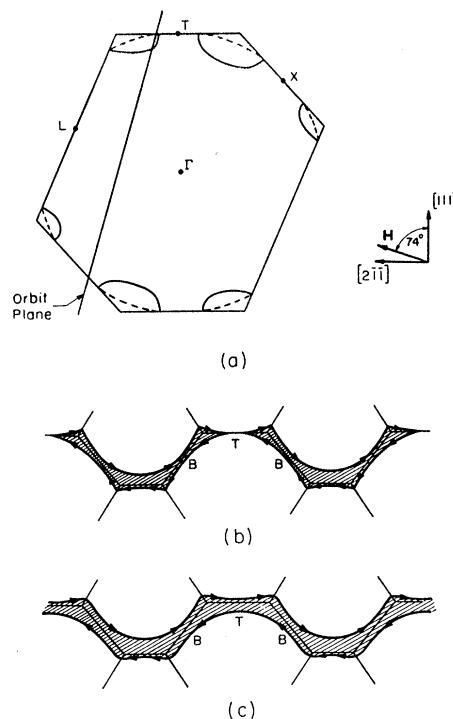


FIG. 15. (a) Section through the center of the Brillouin zone and normal to  $[01\bar{1}]$ . Solid curves indicate hypothetical Fermi surface with necks; dashed lines indicate hypothetical Fermi surface connected like intersecting spheres. (b) Extended closed orbits for surface without necks. (c) Open orbits for surface with necks.

potential near the zone faces, so that it is connected from zone to zone by small necks. The existence of necks means that certain regions of the surface have negative curvature, and thus the carrier whose orbit plane intersects the contact region may not exit through the region, but may simply reverse its direction. This effect is illustrated in Fig. 15, which shows a section through the center of the Brillouin zone normal to  $[01\bar{1}]$ . In the figure the dashed lines indicate the cross section of a spherically shaped surface, while the solid lines represent a surface with necks, which have been exaggerated in size to show the different behavior more clearly. The orbit plane shown is normal to  $\mathbf{H}$  with coordinates  $\phi=0^\circ$ ,  $\theta=90^\circ$ ,  $\psi=16^\circ$ , the effect of necks on the cutoff of open orbits being greatest for this field direction. Figure 15(b) shows the closed orbits in the orbit plane for the case of no necks. Since the plane intersects the breakthrough region on the  $T$  face, the carriers may exit across this face and can thus fold back upon their starting point, creating closed trajectories. When the necks are present, as in Fig. 15(c), the negative curvature of the surface near the  $T$  face allows the carriers to reverse their direction within the zone without exiting across the face. Thus the extended closed orbits of Fig. 15(b) are connected together, giving rise to secondary open orbits along  $[01\bar{1}]$ . In the present instance, the search program would erroneously conclude that no open orbits exist for this orbit plane.

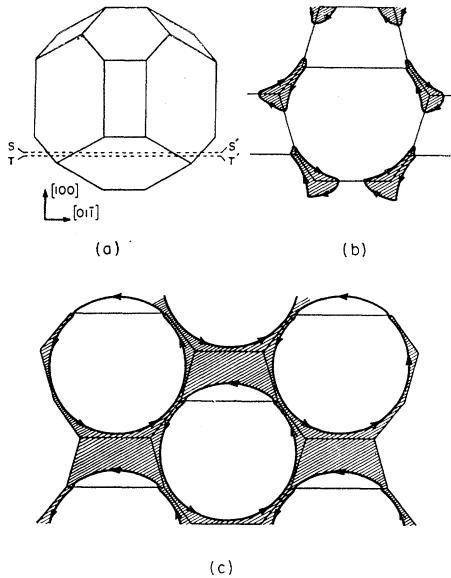


FIG. 16. (a) View of Brillouin zone with (011) face parallel to plane of the figure, showing positions of orbit planes  $SS'$  and  $TT'$  normal to  $[100]$ . (b) Section  $TT'$  showing closed hole orbits. (c) Section  $SS'$  showing closed electron orbits on first-zone hole surface.

Clearly, the factor determining the success of the search program in finding open orbits correctly is the length of the necks as measured normal to the zone faces. For the models considered previously these neck structures appear to be quite small, particularly for the RAPW model. The important consideration is the extent to which these necks affect the cutoff angle for the open orbits found by the search program. For the exaggerated surface shown in Fig. 15, the actual cutoff angle is  $8^\circ$  larger than that found by the search program. For the dHvA model surface, the difference is on the order of  $1^\circ$ . For the other cutoff positions the differences are somewhat less than this, owing to the obliqueness with which the orbit plane intersects the contact regions.

### B. Free-Electron Open Orbits

As a starting point for understanding the type and order of open orbits that may exist on the mercury Fermi surface, it is convenient to consider the free-electron model. It is to be expected that this model will

TABLE V. Angular range of open orbits for free electron and RAPW models.

Open-orbit type	Extent of open orbit	
	Free electron	RAPW
{100}	$-90^\circ \leq \psi \leq 90^\circ$	$-49^\circ \leq \psi \leq 49^\circ$
{011}	$-21^\circ \leq \psi \leq 42^\circ$ $54^\circ \leq \psi \leq 69^\circ$	$-10^\circ \leq \psi \leq 30^\circ$
{102}	$-57^\circ \leq \psi \leq 66^\circ$ $78^\circ \leq \psi \leq 90^\circ$	None

serve as an upper bound on the number of possible open orbits, since there is no breakthrough on the  $B$  and  $T$  faces to limit their existence. Such seems to be the case, since for practically every field direction investigated, orbits extending through more than twelve zones are observed at some position on the Fermi surface. For some directions periodic open orbits up to order five are observed, while for others, closed orbits extending through 78 zones are seen. The major usefulness of the free-electron model is the understanding of the kinds of open orbits that may exist in regions of the stereogram where the magnetoresistance minima vanish. By studying these orbits, it may be learned what modifications must be made in order to obtain agreement with the magnetoresistance data. Table V gives information about the kinds of open orbits observed in the experimentally interesting crystal planes: {100}, {110}, and {102}.

An especially useful example of the information gained from consideration of the free-electron model is seen in the {100} planes. Of particular interest is the intersection of (010), (001), and (011) at the  $[100]$  (real lattice) direction. Along this axis Datars and Dixon<sup>5</sup> indicate that the magnetoresistance should saturate independent of  $\alpha$ , due to the fact that there are two nonintersecting bands of open orbits along (010) and (001) (Table III, case III). Contrary to this finding, the open-orbit search program finds that all three bands of orbits intersect at  $[100]$  to form only closed orbits. In fact, for a certain range of orbit planes normal to  $[100]$ , it finds that only closed *electron* orbits on the hole sheet are allowed. This situation is illustrated in Fig. 16, where two cross sections of a model Fermi surface are considered. This, then, is an example of geometric discompensation analogous to the  $\langle 100 \rangle$  directions in copper; under these conditions the magnetoresistance also saturates independent of  $\alpha$  (Table III, case IV). It is found that no open orbits can be created for the field along  $\langle 100 \rangle$  simply by modifying the free-electron model to include breakthrough on the  $B$  and  $T$  faces. Therefore, for all models of the mercury Fermi surface under consideration, only closed orbits will exist for  $\mathbf{H}$  along  $\langle 100 \rangle$ . However, since the magnetoresistance is found experimentally to saturate for the field in this direction, a major constraint on all models to be investigated is that they exhibit geometric discompensation at  $\langle 100 \rangle$ .

### C. RAPW Open Orbits

As seen in Table V, the range of open orbits is greatly attenuated by the additional breakthrough regions in the RAPW model. It is found that the most important factor in limiting open orbits is the increased  $A$ -face breakthrough and its appearance on the edges of the  $B$  faces. In the free-electron model all open orbits make use of the  $A$ -face contact regions to traverse from zone to zone. Thus it is not surprising that when part of

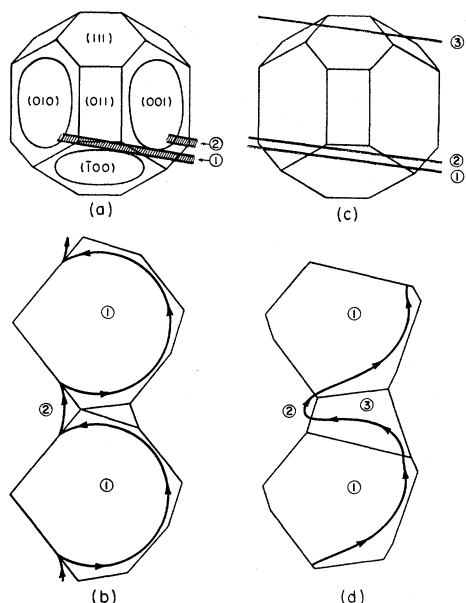


FIG. 17. (a) View of Brillouin zone normal to (011) face showing positions of bands of free-electron secondary open orbits. (b) Free-electron secondary open orbit along  $g_{011}$ . The numbered sections correspond to positions shown in (a). (c) Positions of RAPW tertiary open orbit shown in (d).

this contract boundary is transferred to the  $B$  faces, the free-electron orbits are curtailed. The search program also finds that the introduction of contact on the  $B$  and  $T$  faces does not create additional open orbits, but instead interferes with existing ones. In addition, extended orbits and higher-order open orbits, seen in the free-electron model, do not appear in the RAPW model. Most important, however, is the fact that the RAPW model, under the approximations of the search program, does not agree well with the magnetoresistance results. Open orbits do not exist over a large enough range in  $\{100\}$  planes, while on the other hand, they extend over too great a range in  $\{011\}$  planes. The RAPW model does satisfy the condition necessary to allow  $\langle 100 \rangle$  to be singular field directions. It is found that there is a small band of closed electron orbits on the hole surface for  $\mathbf{H}$  in these directions, the width of this band being less than 1% of the Brillouin zone width.

Several comments should be made concerning open orbits normal to  $\{011\}$  and  $\{123\}$  planes postulated by Datars and Dixon<sup>5</sup> on a modified RAPW model. On such a model they find a secondary open orbit normal to (011) for the field along  $[100]$ . As has been pointed out, no such orbit can exist, since  $[100]$  is a singular field direction. For the field rotated slightly away from  $[100]$  in the (011) plane, a secondary orbit such as the one postulated does exist on the free-electron model, as can be seen from Fig. 17(b). This open orbit depends for its existence upon finding sections of the surface between the breakthrough regions on the  $\langle 100 \rangle$  and

$\langle 001 \rangle$  faces. The existence of such regions allows a carrier to enter on the  $\langle 001 \rangle$  face, orbit on a plane inside the zone without intersecting any other breakthrough regions, and then exit on the  $\langle 010 \rangle$  face. No such sections can be found for an RAPW-type Fermi surface, since the breakthrough regions on  $\langle 100 \rangle$  and  $\langle 001 \rangle$  are connected at the intersection of the two faces, allowing only closed orbits to be produced. Although these secondary orbits are not allowed on the RAPW surface, a band of ternary open orbits is found, as shown in Fig. 17(d); their current direction in  $\mathbf{k}$  space is normal to (011). In addition, the search program does not find the orbits shown by Datars and Dixon for the  $\{123\}$  planes on the free electron or the RAPW model. It may be that the orbit which they exhibit does not satisfy the constraint of lying wholly within one plane.

Investigation of the two other theoretical Fermi surfaces, the dHvA model and the HAA model, show that they likewise are deficient in explaining the magnetoresistance data. The dHvA model, like the RAPW Fermi surface, supports orbits over too great a range in  $\{01\bar{1}\}$  and over too small a range in  $\{100\}$ . On the other hand, the HAA model supports very few open orbits due to the very large regions of contact on the  $B$  faces of the Brillouin zone.

## V. MODEL FERMI SURFACE

Studies on copper<sup>23,24</sup> have shown that detailed topological information about the Fermi surface can be derived from studies of the high-field galvanomagnetic properties. It is not to be expected at this stage of investigation that such detailed conclusions can be drawn for mercury, for which the Fermi surface is considerably more complex. It is interesting nevertheless to consider how far the simple elliptical model of the previous section can be used to interpret the magnetoresistance data.

### A. Breakthrough Regions and Open Orbits

Some indications of the relation between the breakthrough regions and the existence of open orbits have been made previously. It has been shown that certain breakthrough regions are favorable for the existence of orbits, i.e., the carriers use these regions to travel from one zone to the next. Other regions are unfavorable for the existence of the orbits, i.e., their presence changes the open orbits into closed ones. The bands of open orbits are thus determined for a given field direction by orbit planes normal to the field and just tangent to these two types of regions. It is convenient to show the relation between the open orbits and these different types of regions by means of diagrams, such as those shown for  $\{011\}$ -type orbits in Fig. 17. Figure 17(a)

<sup>23</sup> R. V. Coleman, A. J. Funes, J. S. Plaskett, and C. M. Tapp, Phys. Rev. **133**, A521 (1964).

<sup>24</sup> J. R. Klauder, W. A. Reed, G. F. Brennert, and J. E. Kunzler, Phys. Rev. **141**, 592 (1966).

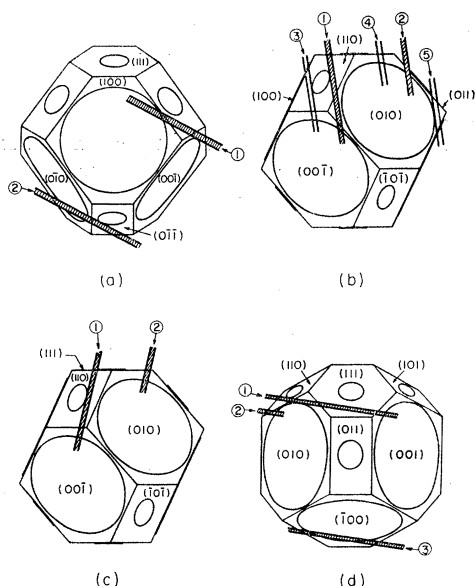


FIG. 18. Positions of MAG V open orbits. (a) Tertiary orbits in (100) near  $\psi=63^\circ$ . (b) Secondary (sections 1 and 2) and quaternary (sections 3, 4, and 5) orbits in (011) near  $\psi=-10^\circ$ . (c) Secondary orbits in (011) near  $\psi=16^\circ$ . (d) Quaternary orbits in (011) near  $\psi=80^\circ$ .

gives a view of the Brillouin zone along the normal to (011), so that field directions in (011) are represented by lines in the plane of the figure. Thus the orbit planes are normal to the plane of the figure, intersecting the zone in the shaded sections shown. The intersection of a typical orbit plane lying in section one is shown in Fig. 17(b) and designated also by the number 1. The carrier moving on the trajectory shown in this first zone exits into a second zone, which adjoins the first on the (010) face. Rather than showing the intersection of the orbit plane with this second zone in a separate figure, it is more convenient instead to indicate its equivalent position in the first zone. Thus, in Fig. 17(a) sections one and two represent the same set of orbit planes intersecting adjoining zones in different positions. This convention will be used in the rest of what follows to indicate the location of open-orbit planes in the repeated zone scheme.

The motion of the secondary orbit of Fig. 17(b) can be simply described using this convention and the nomenclature introduced previously (see Fig. 14). A carrier orbiting in zone (000) on a plane in section one, exits into zone (010) and orbits on a plane in section two. It then exits this zone into zone (011) and orbits on a plane in section one. Thus the carrier alternates from one section to the other as it travels along the normal to (011), i.e., the plane of Fig. 17(a). The widths of these sections or bands of open orbits are determined by the relative positions of the favorable and unfavorable breakthrough regions. In the example shown the favorable regions for section one lie on the (010) and (00 $\bar{1}$ ) faces [the latter lies just beneath the former in

Fig. 17(a)]. The unfavorable regions lie on ( $\bar{1}00$ ) and (001), and planes tangent to these regions, normal to the plane of the figure, determine the limits of open-orbit existence. As the field is tilted toward [100], i.e., counterclockwise in the plane of the figure, this band of orbits becomes progressively smaller, finally vanishing for the field along [100]. At this point there exists a single-orbit plane tangent to both the ( $\bar{1}00$ ) and the (001) regions, both of which are unfavorable. Similarly, if the field is rotated in the other direction, away from [100], the width of the band vanishes when there exists a single orbit plane tangent to the (010) region (favorable) and the ( $\bar{1}00$ ) region (unfavorable). In general, for all types of open orbits observed on the mercury Fermi surface, the problem of determining the field directions for which the open orbits vanish depends upon finding the location of orbit planes just tangent to both a favorable and an unfavorable breakthrough region, or to two unfavorable regions.

To determine a model best fitting the magneto-resistance data, the above considerations have been applied to the elliptical model for orbit planes normal to the four field orientations where the deep minima of the rotation diagrams vanish. The four parameters of this model have been varied such that the tangency conditions are satisfied simultaneously at these four orientations. Such a model is unique in the sense that no other set of the parameters gives simultaneous cutoff at the four positions. The sizes of the breakthrough regions for this model, designated MAG V, are indicated in Fig. 3 and Table II.

## B. Empirical Model

A complete derivation of the MAG V model will not be attempted here. Only the nature of the open and extended orbits will be discussed, with particular attention being paid to the relation between surface topology and cutoff of the open orbits. This relationship is most complicated for the field near cutoff ( $\psi=63^\circ$ ) in (100), where eight different breakthrough regions are involved in the determination of the open orbits. In the free-electron model, three different orders of orbits normal to (100) exist near cutoff. Introduction of breakthrough on the *B* and *T* faces of the zone, and enlargement of the *A*-face breakthrough, reduces the number of orders involved to one. The resulting ternary band of orbits on the MAG V surface is indicated in Fig. 18(a). Breakthrough regions favorable for the existence of these orbits occur on (100), ( $\bar{1}00$ ), (010), and (0 $\bar{1}0$ ). The band is seen to lie on two sections of the Fermi surface, its width being limited by the unfavorable region on (00 $\bar{1}$ ) in section one, and by the unfavorable region on (0 $\bar{1}\bar{1}$ ) in section two. This band vanishes when a single orbit plane is just tangent to these two regions for  $\psi=63^\circ$ . Inspection of the model indicates that first-order open orbits exist only in the range from  $\psi=0^\circ$  to  $\psi=54.63^\circ$ , at which point **H** is

along  $[100]$ . For  $\psi$  larger than the latter value only the ternary orbits exist and are responsible for the observed magnetoresistance minima.

The next most complicated situation occurs near cutoff for  $\psi = -10^\circ$  in  $(01\bar{1})$ . Two orders of orbits, secondary and quaternary, are involved as shown in Fig. 18(b). The cross-hatched regions in the figure indicate the positions of the secondary orbits, which are directed along  $[01\bar{1}]$  as indicated by Fig. 15(c). A carrier in this orbit enters the  $(00\bar{1})$  face and exits on  $(0\bar{1}0)$  in section one, and then enters the  $(010)$  face of the adjoining zone in section two, exiting again on  $(001)$  to complete the period of motion. The width of this band of orbits is limited in section one by unfavorable breakthrough regions on  $(110)$  and  $(101)$ , and in section two by the  $(011)$  region.

The unshaded sections three, four, and five in Fig. 18(b) indicate the positions of the quaternary orbits, which are also along  $[01\bar{1}]$ . The motion in this orbit is similar to the secondary orbit, except that now a carrier entering the  $(00\bar{1})$  face in section three exits through the opening in  $(100)$  and enters the adjoining zone on section five. In this zone it can only leave through the other exit point on  $(\bar{1}00)$  and return to the original zone on section three. The remainder of the motion resembles the secondary orbit with the carrier exiting on  $(0\bar{1}0)$  to the adjoining zone on section four. The width of the band of quaternary orbits is limited by the same unfavorable regions as limit the secondary orbits. Both bands vanish for  $\psi = -10^\circ$ , when a single-orbit plane can be found tangent to the breakthrough on  $(110)$  in one zone and to the breakthrough on  $(011)$  on the zone adjoining the  $(00\bar{1})$  face of the first.

As the field is rotated in  $(01\bar{1})$  from  $\psi = -10^\circ$  to  $\psi = 16^\circ$ , the width of the quaternary band of orbits begins to be limited by the breakthrough region on  $(010)$ . At the same time, some of these orbits in section three no longer intersect the  $(100)$  breakthrough. Such orbits cease to travel on section five and become second-order orbits, circulating on sections three and four. Eventually this change becomes complete, and the band of quaternary orbits is replaced by a band of secondary orbits resembling those in sections one and two. As the field continues to be rotated [clockwise in Fig. 18(b)], both sets of secondary orbits become limited in width by the breakthrough regions on  $(111)$  and  $(110)$ . This effect is shown for one of these sets in Fig. 18(c). All the orbits vanish for  $\psi = 16^\circ$  when a single orbit plane can be found tangent to both of these regions.

For the field lying in  $(011)$  only quaternary orbits exist in the MAG V model, their trajectory being similar to the ternary orbits shown in Fig. 17(d) for the RAPW model. In this case, however, the carrier travels from section three back into section one and then into section two, thus making the order of the orbit higher than in the RAPW model. The positions of the band of quaternary orbits on the MAG V model are shown in

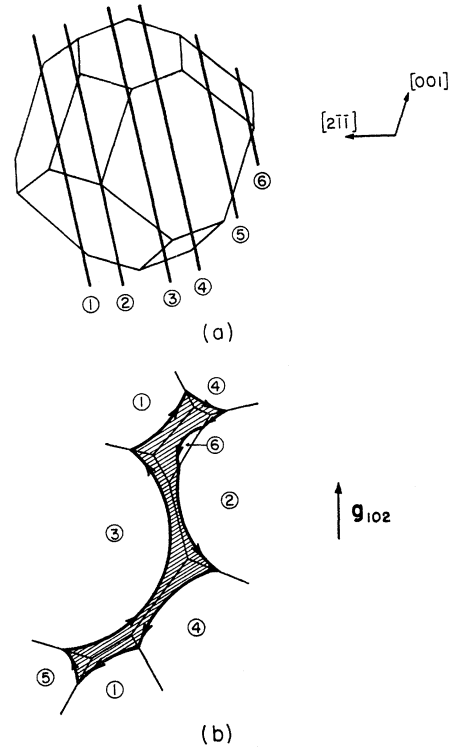


FIG. 19. (a) View of Brillouin zone along  $g_{102}$  showing positions of extended orbit in MAG V model. (b) Extended orbit in MAG V model. The scale of drawing for both (a) and (b) is equal.

Fig. 18(d). Regions favorable for its existence in section one are  $(001)$ ,  $(0\bar{1}0)$ , and  $(100)$ , while the unfavorable regions are  $(110)$ ,  $(010)$ , and  $(00\bar{1})$ . The band vanishes for  $\psi = 79^\circ$ , when a single orbit plane can be made tangent to  $(00\bar{1})$  and  $(110)$ , and for  $\psi = 90^\circ$ , when the orbit plane is tangent to both  $(010)$  and  $(001)$ . At the latter orientation, the field lies along  $[100]$ , which as shown previously, must be a singular field direction. This requirement is satisfied by the MAG V model; the electron orbits on the hole surface have been shown previously in Fig. 16.

It is important to determine the over-all uncertainty in the dimensions for the empirical model. Considering the experimental error, the assumptions about necks and the elliptical shape of the breakthrough regions, it is estimated that dimensions given in Table II for MAG V are accurate only to within  $\pm 5\%$ . In the pseudopotential fit more importance will thus be given to fitting the experimental dHvA areas than the dimensions given here.

### C. Extended Orbits

Since it has been shown that the MAG V model explains the existence and range of deep minima observed experimentally, it is now interesting to investigate the regions of the stereogram where the less pronounced minima occur, i.e., the dashed lines in Fig. 13. When the parameters of the MAG V model are placed into the

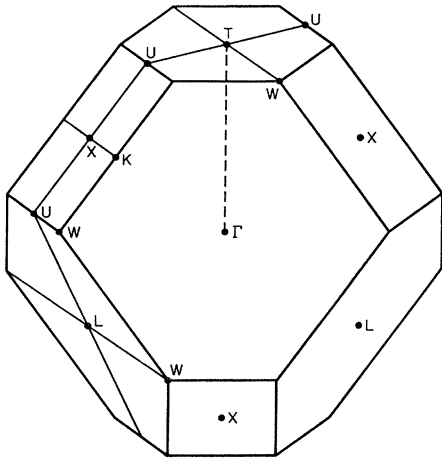


FIG. 20. Symmetry points of the mercury Brillouin zone.

computer search program and these regions investigated, no open orbits are discovered. What is found instead is a number of types of extended orbits, an example of which is shown in Fig. 19. For the field magnitudes used in the experiments it is estimated that the perimeter of these orbits in real space is on the order of one or two mean-free-path lengths. This suggests that the broad, shallow minima observed experimentally are associated with these extended orbits, for which the condition  $\omega_{c\tau} \gg 1$  is not satisfied. Several criticisms of such an association can be made, however. When the search program investigates a region duplicating that where a broad minimum is observed experimentally, it is found that the extended orbits exist over a much larger range of rotation angle,  $\theta'$ , than the breadth of the minimum itself. This may be partially explained by noting that the character of the extended orbits changes as the rotation angle changes, so that the effective current direction for the orbits may be a rapidly varying function of  $\theta'$ . For a given  $\mathbf{J}$  within the sample, only a fraction of the extended orbits excited as the field is rotated may have the proper current direction to be observed. Thus, the minima observed in (102) and (125) may be due to the same region of extended orbits, but with different effective current directions.

Another criticism of this association comes from the fact that the effective current direction for an extended orbit would be expected to be very dependent upon the temperature and the magnitude of the field. Thus, it might be expected that minima due to such orbits would be quite dependent upon these quantities, which does not appear to be the case for the broad minima observed. It is likely that the appearance of these minima does not have a simple geometrical interpretation, but depends in a complicated fashion on the anisotropy of the scattering mechanism as well as the topology of the Fermi surface. In any case, if it is assumed that their observation does not demand the existence of open orbits, then the MAG V model retains

its validity and can be used as a starting point for the pseudopotential calculations to be described next.

## VI. PSEUDOPOTENTIAL CALCULATION

In order to compare the empirical model with the results of the dHvA experiments, it is necessary to calculate the detailed shapes of extremal orbits on the Fermi surface. Such a determination requires a band-structure calculation with adjustable parameters giving a calculated Fermi surface having its breakthrough dimensions fitted to those of MAG V. Since these dimensions are not directly observed by experiment and their uncertainty is relatively large, it appears more meaningful to place stronger weight on fitting the dHvA areas. Thus, in the pseudopotential calculation described here, an attempt has been made to fit only one of the breakthrough dimensions, while simultaneously fitting two extremal areas on the first zone sheet to the observed dHvA frequencies. The fitting procedure is similar to that used in the dHvA model, except that in this case the spin-orbit coupling is included explicitly as a third fitting parameter and the Fermi level is adjusted to maintain charge compensation.

The pseudo wave function for this calculation is taken to be a linear combination of the eight plane waves used in the HAA model. These waves are chosen in order to take into account the fourfold degeneracy of the free-electron states for the point  $W$  at the corner of the mercury Brillouin zone (see Fig. 20). If the pseudopotential is assumed to be a local operator, then matrix elements of the form  $\langle \mathbf{k} + \mathbf{g}' | W | \mathbf{k} + \mathbf{g} \rangle$  depend only upon the wave vector,  $\mathbf{G}$ , where  $\mathbf{G} = \mathbf{g}' - \mathbf{g}$ , and these matrix elements may be designated by the notation,  $W_{\mathbf{G}}$ . For the eight plane waves used in this calculation, three matrix elements are seen to be involved, namely,  $W_{001}$ ,  $W_{011}$ , and  $W_{111}$ . As has been done in the dHvA model, it will be assumed that  $W_{110} = W_{111}$ , since the magnitudes of  $\mathbf{g}_{110}$  and  $\mathbf{g}_{111}$  are equal to within  $\frac{1}{2}\%$ .

Inclusion of spin-orbit coupling in the problem can be made in several ways.<sup>25-28</sup> In this case we use the formulation given by Animalu,<sup>15</sup> who has shown that the matrix elements of the total pseudopotential,  $W_T$ , may be expressed in the form

$$\langle \mathbf{k} + \mathbf{g}', \chi' | W_T | \mathbf{k} + \mathbf{g}, \chi \rangle = \langle \mathbf{k} + \mathbf{g}' | W | \mathbf{k} + \mathbf{g} \rangle \delta_{\chi, \chi'} + \langle \mathbf{k} + \mathbf{g}', \chi' | W_{SO} | \mathbf{k} + \mathbf{g}, \chi \rangle. \quad (1)$$

Here  $\chi$  refers to the spin state,  $W$  is the usual pseudopotential without spin, and  $W_{SO}$  is the spin-orbit term. Matrix elements of  $W_{SO}$  are found to be of the form

$$\langle \mathbf{k} + \mathbf{g}', \chi' | W_{SO} | \mathbf{k} + \mathbf{g}, \chi \rangle = \langle \chi' | i \mathbf{s} \cdot (\mathbf{k} + \mathbf{g}) \times (\mathbf{k} + \mathbf{g}') q | \chi \rangle, \quad (2)$$

<sup>25</sup> J. R. Anderson and A. V. Gold, Phys. Rev. **139**, A1429 (1965).

<sup>26</sup> Gideon Weisz, Phys. Rev. **149**, 504 (1966).

<sup>27</sup> L. M. Falicov and Stuart Golin, Phys. Rev. **137**, A871 (1965).

<sup>28</sup> D. Brust, Phys. Rev. **134**, A1337 (1964).

where

$$q = 24\pi(\lambda_1 - \lambda_2)q_1 + (8\pi/\Omega G^2)\lambda_2 R_M^3 |\mathbf{k} + \mathbf{g}'| |\mathbf{k} + \mathbf{g}| j_2(GR_M), \quad (3)$$

and

$$q_1 = \frac{1}{\Omega} \int_0^{R_M} j_1(|\mathbf{k} + \mathbf{g}'| r) j_1(|\mathbf{k} + \mathbf{g}| r) r^2 dr. \quad (4)$$

In these equations,  $\lambda_1$  and  $\lambda_2$  represent the strength of spin-orbit coupling from  $p$  and  $d$  states, respectively, while  $R_M$  is related to the radius of the inner core and for mercury has the value  $R_M = 2.6$  a.u. It is seen that the spin-orbit part of the potential is  $\mathbf{k}$ -dependent

through the cross-product factor and the spherical Bessel functions. In what follows it will be convenient to write the spin-orbit matrix elements in the form

$$\langle \mathbf{k} + \mathbf{g}', \chi' | W_{so} | \mathbf{k} + \mathbf{g}, \chi \rangle = \langle \chi' | i\boldsymbol{\sigma} \cdot \mathbf{Q}(\mathbf{g}', \mathbf{g}) | \chi \rangle. \quad (5)$$

With this expression for the matrix elements, the Hamiltonian matrix to be diagonalized can be written as

$$H = \begin{bmatrix} A & B \\ -B^* & A^* \end{bmatrix}. \quad (6)$$

The matrices  $A$  and  $B$  are given by

$$A = \begin{bmatrix} |\mathbf{k}|^2 & W_{001} + iQ_z^{0,1} & W_{011} + iQ_z^{0,2} & W_{111} + iQ_z^{0,3} \\ W_{001} - iQ_z^{0,1} & |\mathbf{k} + \mathbf{g}_{001}|^2 & W_{001} + iQ_z^{1,2} & W_{011} + iQ_z^{1,3} \\ W_{011} - iQ_z^{0,2} & W_{001} - iQ_z^{1,2} & |\mathbf{k} + \mathbf{g}_{011}|^2 & W_{001} + iQ_z^{2,3} \\ W_{111} - iQ_z^{0,3} & W_{011} - iQ_z^{1,3} & W_{001} - iQ_z^{2,3} & |\mathbf{k} + \mathbf{g}_{111}|^2 \end{bmatrix}, \quad (7)$$

$$B = \begin{bmatrix} 0 & iQ_x^{0,1} + Q_y^{0,1} & iQ_x^{0,2} + Q_y^{0,2} & iQ_x^{0,3} + Q_y^{0,3} \\ -iQ_x^{0,1} - Q_y^{0,1} & 0 & iQ_x^{1,2} + Q_y^{1,2} & iQ_x^{1,3} + Q_y^{1,3} \\ -iQ_x^{0,2} - Q_y^{0,2} & -iQ_x^{1,2} - Q_y^{1,2} & 0 & iQ_x^{2,3} + Q_y^{2,3} \\ -iQ_x^{0,3} - Q_y^{0,3} & -iQ_x^{1,3} - Q_y^{1,3} & -iQ_x^{2,3} - Q_y^{2,3} & 0 \end{bmatrix},$$

where the coordinate axes are defined by Fig. 4(a). In specifying the components of  $Q(\mathbf{g}', \mathbf{g})$  it has been convenient to designate  $\mathbf{g}_{000}$ ,  $\mathbf{g}_{001}$ ,  $\mathbf{g}_{011}$ , and  $\mathbf{g}_{111}$  as 0, 1, 2, 3, and to set  $Q_z(\mathbf{g}_{001}, \mathbf{g}_{011}) = Q_z^{1,2}$ , for example. To calculate  $E(\mathbf{k})$  the Hamiltonian matrix has been diagonalized using standard computer techniques; for each  $\mathbf{k}$  vector there are four doubly degenerate eigenvalues as required by time-reversal symmetry. For a given set of the three fitting parameters  $W_{001}$ ,  $W_{011}$ , and  $\lambda_1$  ( $\lambda_2 = 0$ ), extremal orbits on the Fermi surface are found by a simple search procedure that brackets the Fermi energy, and then finds the magnitude of the  $\mathbf{k}$  vector on the Fermi surface in a given direction by interpolation. To ensure that the Fermi surface found by this procedure is compensated, the Fermi level is adjusted for every set of the fitting parameters using the method of Harrison.<sup>10</sup> This method takes into account the distortion of the free-electron sphere due to  $W_{001}$  and  $W_{011}$ . The spin-orbit parameter also affects the compensation, but the resulting shift in energy cannot be simply expressed in closed form. Consequently, it has not been included in the determination of the Fermi level; it is estimated that neglect of this effect causes a lack of compensation of less than 1%.

The breakthrough dimension most sensitive to shifts in the Fermi level is the intercept along  $XK$ , i.e., the parameter  $a_B$  in the MAG V model. Since the area of the orbit depends critically on this dimension, it is advantageous to hold it fixed at the value determined by MAG V while varying the fitting parameters to obtain agreement with the dHvA frequencies. The extremal areas investigated are those of the  $\beta$  and  $\tau$  orbits on the first-zone surface (see Fig. 2) and the  $\alpha$

orbit on the second-zone surface. The latter orbit corresponds to the minimum cross section of the disk on the (100) zone face, i.e., its area is calculated for  $\mathbf{H}$  along  $[01\bar{1}]$ . For the  $\beta$  orbit the area is computed for the field along  $[100]$ , while the area of the  $\tau$  orbit corresponds to  $H$  along  $[01\bar{1}]$ .

Several schemes have been used to fit pseudopotential coefficients to experimental information on metallic Fermi surfaces.<sup>25-28</sup> Previous work on mercury<sup>1</sup> has shown that it is not possible to fit all the experimental dHvA frequencies simultaneously to within the accuracy of the measurements (2%) using only two parameters. It is not to be expected that the inclusion of an additional fitting parameter will make a fit possible in the present instance, particularly with the additional constraints on compensation and the value of the breakthrough dimension along  $XK$ . The approach taken here is one of investigating a large portion of parameter-space to find regions giving reasonable agreement between the dHvA and magnetoresistance experiments. The search for these regions has been carried out for various fixed values of  $\lambda_1$ , while observing the variation of the extremal areas as a function of  $W_{001}$  and  $W_{011}$ . The model potential of Animalu includes an additional spin-orbit parameter  $\lambda_2$  for the  $d$ -wave interaction [see Eq. (3)]. Preliminary investigations indicate that its effect on the Fermi surface is small, and it has thus been set to zero for convenience. The signs of the pseudopotential coefficients have been taken to agree with the theoretical values determined by Animalu and Heine,<sup>13,15</sup> for which  $W_{001} < 0$ , and  $W_{011}$ ,  $\lambda_1 > 0$ . To keep  $a_B$  at its proper value and the area of the  $\beta$  orbit within 2% of its experimental value, it is found that



TABLE VI. Pseudopotential coefficients (in Ry).

Model	$W_{100}$	$W_{110}$	$W_{111}$	$\lambda_1$
dHvA	-0.066	0.047	0.047	0.00
HAA	-0.025	0.065	0.065	0.10
8 PW	-0.018	0.028	0.028	0.16

$W_{001}$  cannot be taken less than  $-0.062$  Ry. With this constraint satisfied, an exact fit to the area of the  $\beta$  orbit and to  $a_B$  can be found for every value of  $\lambda_1$  with  $W_{011}$  in the range  $0.024 \leq W_{011} \leq 0.045$  Ry.

With the assumption that the optimum values for the coefficients lie in this region of parameter space, the final fit is determined by the areas of the  $\alpha$  and  $\tau$  orbits. It is found that the  $\alpha$  orbit is essentially insensitive to  $\lambda_1$ , depending most strongly on the value of  $W_{001}$ . This behavior is to be expected since the second-zone surface exists only on  $\{001\}$  faces. The  $\tau$  orbit, however, depends strongly on all the parameters, since it exists on a portion of the surface involving all three types of zone faces. For most values of the fitting parameters in the above range it is found that the area of the  $\alpha$  orbit is larger, and the area of the  $\tau$  orbit smaller, than the experimental values, as is the case for both the RAPW and dHvA models. By letting  $W_{001}$  lie outside the range given above, the  $\alpha$  orbit may be fitted exactly for  $W_{001} = -0.074$  Ry. It is impossible, however, to obtain a simultaneous fit of the  $\alpha$  and  $\beta$  orbits with the constraint on the dimension  $a_B$ . The best fit for the  $\alpha$  orbit with the parameters in the above range is obtained for  $\lambda_1 = 0$ , with  $W_{001}$  and  $W_{011}$  taking on the

values used for the dHvA model (see Table VI), in which case the area is 12% larger than the experimental value. Such a result seems to imply that the third fitting parameter is ineffective for the second-zone sheet. Since the parameter  $\lambda_1$  is a relativistic one, this situation is not too surprising because the RAPW also cannot fit this area to better than 16%. The second-zone surface extends some distance into the second zone and it is possible that it is more strongly influenced by higher-order plane waves than the first-zone surface. Inclusion of these additional states may allow a simultaneous fit to the Fermi-surface dimensions in both zones.

The introduction of the spin-orbit coefficient does improve agreement between the calculated and experimental areas for the  $\tau$  orbits. With  $\lambda_1 = 0$  and the other coefficients taking on the values used to produce the dHvA model, the area of the  $\tau$  orbit is 28% smaller than the experimental quantity. This discrepancy diminishes as  $\lambda_1$  is increased in magnitude, the other parameters being chosen to give an exact fit to the area of the  $\beta$  orbit and  $a_B$ . On the other hand, the difference between the computed and experimental areas of the  $\alpha$  orbit becomes larger. The best compromise occurs when  $\lambda_1 = 0.030$  Ry, with  $W_{001} = -0.062$  Ry and  $W_{011} = 0.042$  Ry, in which case there is a 20% error in both areas. It is perhaps more meaningful to attempt to fit only the features of the first-zone surface and to omit further consideration of the  $\alpha$  orbits. In this case it is possible to obtain simultaneously an exact fit for the areas of the  $\beta$  and  $\tau$  orbits and the dimension  $a_B$  with the coefficients in the following range:  $-0.030 \leq W_{001} \leq -0.015$  Ry,  $0.0266 \leq W_{011} \leq 0.0277$  Ry, and  $0.156 \leq \lambda_1 \leq 0.159$  Ry. For values of  $\lambda_1$  greater than this upper bound, it is found that  $W_{011}$  must be taken to be quite small in order to fit the  $\beta$  orbit. When this is done the Fermi surface no longer contacts the  $T$  face, and thus the  $\tau$  orbits are destroyed. The final values of the fitting parameters (see Table VI) are taken to be those lying in the above range and giving the best fit to the remainder of the dimensions of the MAG V surface.

Energy bands calculated for the final set of pseudopotential coefficients are shown in Fig. 21. Although they bear some resemblance to the RAPW bands, it is not possible to obtain similar Fermi surfaces for the two models by simply shifting the position of the Fermi level. To obtain a compensated surface for the pseudopotential bands, the Fermi level must be taken at a value of 0.522 Ry, only slightly lower than the free-electron value. This produces a model Fermi surface (designated 8 PW) which is topologically equivalent to those discussed in Sec. II. The breakthrough dimensions calculated for this surface are given in Table II, and the extremal areas are listed in Table VII. It is seen that the dimensions  $b_B$  and  $r_T$  for the 8-PW model are substantially smaller than those for MAG V, and do not lie within the error limits necessary to give the

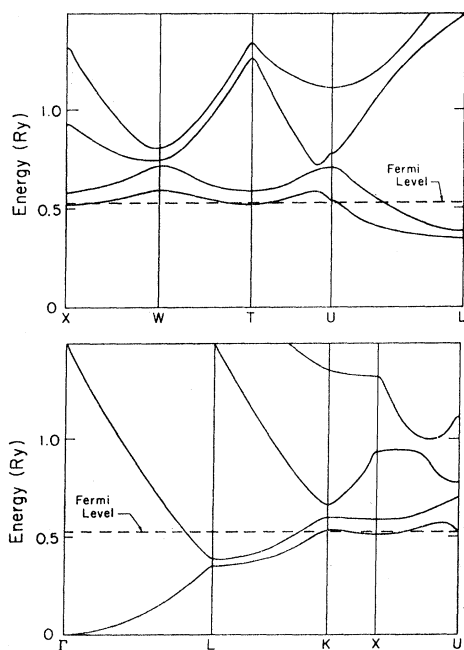


FIG. 21. Energy bands for the 8-PW model along various symmetry directions.

proper cutoff for the observed open orbits. This is not too surprising, since the fitting procedure places stronger weight on obtaining agreement with the dHvA areas. It is likely that the introduction of additional plane waves, and thus additional pseudopotential coefficients, would allow an improved fit to all the first-zone dimensions and extremal areas. In the second zone the computed dimensions for the disk are:  $0.44 \text{ \AA}^{-1}$  along  $\mathbf{g}_{100}$ ,  $1.28 \text{ \AA}^{-1}$  along  $[011]$ . These values are larger than the experimental lengths measured by the magnetoacoustic effect<sup>29</sup>:  $0.36 \text{ \AA}^{-1}$  along  $\mathbf{g}_{100}$ , and  $1.13 \text{ \AA}^{-1}$  along  $[011]$ . This discrepancy is to be expected because of the poor fit to the  $\alpha$  orbit for the 8-PW model. Finally it should be noted that definite neck regions exist on the 8-PW surface, but they are small enough that the assumptions of the open-orbit search program are valid to within the approximations used. *Note added in proof.* It now appears likely that the failure of the 8-PW model is due to its neglect of the proximity of the  $5d$  band relative to the conduction band (see Ref. 6). This effect could be taken into account by using a nonlocal pseudopotential similar to that employed by Stark and Falicov in their fits to the Fermi surfaces of zinc and cadmium [see Phys. Rev. Letters **19**, 795 (1967)].

The large value for  $\lambda_1$  found in the eight-plane-wave fit does seem to indicate that relativistic effects are important in crystalline mercury. As in the case of lead, the empirical value for  $\lambda_1$  is substantially larger than the theoretical value calculated by Animalu. With the large discrepancy in the second zone, however, the fitting coefficients must be regarded only as convenient parameters for describing the shape of the first-zone sheet, and probably no deeper theoretical meaning should be ascribed to them.

## VII. CONCLUSIONS

The results of these investigations indicate that mercury is a compensated metal with a two-sheet Fermi surface, consisting of disk-shaped elements in the second zone and an open, multiply connected sur-

<sup>29</sup> T. E. Bogle, C. G. Grenier, and J. M. Reynolds, Bull. Am. Phys. Soc. **12**, 183 (1967).

TABLE VII. Comparison of extremal areas for model Fermi surfaces with experimental dHvA areas.

Model	Extremal area ( $\text{\AA}^{-2}$ )		
	$\alpha$	$\beta$	$\tau$
Experimental	0.305	0.070	0.151
dHvA—3 PW	0.344	0.070	0.107
RAPW	0.354	0.070	0.132
8 PW	0.423	0.070	0.151

face in the first zone. The latter contacts all faces of the fundamental Brillouin zone, and a unique model of these contact regions can be derived from the magnetoresistance data. Calculations of the energy bands using the pseudopotential method also give rise to a Fermi surface with the same general features. It is not possible, however, to obtain a detailed fit to all the dimension of the contact regions deduced from the magnetoresistance data, nor to the extremal area observed in the dHvA measurements. Further theoretical calculations are needed to improve the fit and to resolve the discrepancy between the dimensions of the first- and second-zone surfaces.

Since the dimensions of the Fermi surface deduced from the magnetoresistance measurements are determined indirectly, additional experiments, such as the magnetoacoustic effect or the Gantmakher size effect, are needed to obtain primary determination of these quantities. Measurements of the other galvanomagnetic coefficients, particularly along the singular field direction and in higher magnetic fields, can furnish additional geometrical information about the Fermi surface and perhaps explain the origin of the shallow minima observed in the magnetoresistance rotation diagrams.

## ACKNOWLEDGMENTS

Thanks are due to Dr. G. B. Brandt for much helpful advice concerning the growth and orientation of mercury single crystals. Helpful discussions are acknowledged with Dr. R. D. Pierce, Dr. S. Golin, and Dr. J. H. Condon. A. Adams and H. Lefke deserve special mention for their part in constructing the experimental apparatus.